Mesoscopic Oxide Double Layer as Electron Specific Contact for Highly Efficient and UV Stable Perovskite Photovoltaics

Mohammad Mahdi Tavakoli[1,2], Fabrizio Giordano[1], Shaik Mohammed Zakeeruddin[1], Michael Grätzel[1]*

[1]*Institut des Sciences et Ingénierie Chimiques, Ecole Polytechnique Fédérale de Lausanne (EPFL), EPFL–BCH, CH–1015 Lausanne, Switzerland*

[2]*Department of Materials Science and Engineering, Sharif University of Technology, 14588 Tehran, Iran*

Abstract

The solar to electric power conversion efficiency (PCE) of perovskite solar cells (PSCs) has recently reached 22.7 % exceeding that of competing thin film photovoltaics and the market leader polycrystalline silicon. In order to augment the PCE further towards the Shockley Queisser limit of 33.5 %, judicious engineering of the interfaces between the light harvesting perovskite and the charge carrier extraction layer is warranted. Here, we introduce a mesoscopic oxide double layer as an electron selective contact consisting of a scaffold of TiO_2 nanoparticles covered by a thin film of amorphous SnO_2 (a-SnO_2). The conduction band of a-SnO_2 is well-aligned with the perovskite light harvester as compare to that of the crystalline tetragonal polymorph SnO_2. This accelerates carrier extraction with respect to the bare scaffold, avoiding electron trapping by TiO_2 surface states. As a result, the notorious hysteresis in the current-voltage (*J-V*) curves of PSCs is suppressed and nonradiative carrier recombination retarded

resulting in a remarkable increase of the open circuit photovoltage (V_{oc}). These benefits are specific to a-SnO_2 and disappear upon its crystallization. By introducing the a-SnO_2 coated mp-TiO_2 scaffold as electron extraction layer, we not only increase the V_{oc} and PEC of the device but render it resistant to UV light which forebodes well for outdoor deployment of these new PSC architectures.

Keywords: Electron specific contact, Amorphous SnO_2, Mesoscopic structure, Efficiency, UV stability.

Organic-inorganic perovskite solar cells (PSCs) have been the focus of intensive research during the past few years. So far, compositional engineering and interface modifications have been employed in order to boost the solar to electric power conversion efficiency (PCE) of perovskite solar cell over 22%.[1-6] Surface modification of the electron extraction layer (EEL) is one of the most effective way to improve the efficiency of perovskite solar cell.[4-6] TiO_2 is the most common EEL for fabrication of PSCs due to its low cost, eco friendliness, ease of fabrication and favorable conduction band alignment with the perovskite. However, the compact TiO_2 (c-TiO_2) layer has a relatively low electron mobility and contains electron traps that retard electron extraction leading to enhanced hysteresis in the current-voltage (*J-V*) curves and nonradiative charge carrier recombination .[7-11] To tackle this problem, an additional layer of mesoporous TiO_2 (mp-TiO_2) consisting of a 3-dimensional (3D) array of interconnected TiO_2 nanocrystals is usually deposited on top of the c-TiO_2. However, this EEL structure may bring other risks, such as performance degradation by UV light. Surface modification of mp-TiO_2 scaffold offers an effective way to improve the carrier collection and in turn the photovoltaic metrics of the PSCs.[12-15] For instance, lithium treatment of mp-TiO_2 can help to passivate the surface defects of the EEL and improve the charge collection, resulting in a higher V_{oc} and PCE.[16]

TiO_2 films show photocatalytic activity under UV light,[17,18] which could affect the perovskite. Therefore, TiO_2 layers are increasingly replaced by SnO_2 films which are photo-catalytically inactive, show very high electron mobility and fast electron extraction.[19-21] Methods for depositing SnO_2 based EELs employ *e.g.* solution processing, atomic layer deposition (ALD), and sputtering technique.[22-25] Solution processing has so far yielded the highest PCE of 21.6% reported by Jiang *et al.* albeit on a tiny device area of only 0.0737 cm^2.[26] It appears that the direct deposition of the SnO_2 layer onto the FTO glass is not well reproducible due to the roughness of the conductive glass support,[27] and there is a risk of infiltration with fluoride ions from the FTO. Therefore, Lee *et al.* introduced a compact TiO_2 layer between the FTO and the SnO_2 film attaining a maximum PCE of 19.8%.[15] Dong *et al.* employed SnO_2 quantum dots (NC-SnO_2) mixed with mp-TiO_2 nanoparticles as an EEL for PSCs reporting PSC of 16%.[28] In addition, Song *et al.* deposited a thin layer of SnO_2 on top of anodized amorphous TiO_2 (a-TiO_2), yielding a PCE of 21.1%.[27] While none of these results were certified, they concur that using SnO_2 as EEL the photovoltaic performance and stability are increased with decreasing the undesirable hysteresis effect.[29-31]

Here we introduce a mesoscopic oxide double layer as an electron selective contact consisting of a scaffold of TiO_2 nanoparticles coated by a thin film of amorphous SnO_2 (a-SnO_2) using solution deposition. The band gap of the a-SnO_2 exceeds that of the crystalline tetragonal polymorph by 0.05 eV, affording perfect alignment of its conduction band with that of the perovskite light harvester. This accelerates carrier extraction with respect to the bare TiO_2 scaffold, avoiding electron trapping by surface states. As a result, the notorious hysteresis in the current-voltage curves of PSCs is suppressed and nonradiative carrier recombination retarded yielding a very high open circuit photovoltage (V_{oc}) of 1.2 V. Results from intensity modulated photovoltage

spectroscopy (IMVS) are consistent with these extraordinarily high V_{oc} values. Importantly, we find that these benefits are specific to a-SnO_2 and are not observed upon converting it to a crystalline form by high temperature annealing. Apart from enhancing the photovoltaic performance, the a-SnO_2 coating also prevents UV degradation of the PSC devices based on a-SnO_2/mp-TiO_2 as EEL retaining 97% of their initial PCE after 60 h exposure to the UV light.

Result and discussions

Figure S1 shows a schematic of the investigated device structure. It consisted of FTO glass coated by a compact TiO_2 layer, a 150 nm-thick mp-TiO_2, a thin layer of SnO_2, a 300 nm-thick perovskite film, a 150 nm-thick spiro-OMeTAD hole transfer layer (HTL), and a 80 nm thick gold contact. The mesoporous TiO_2 scaffold was coated in a manner by a conformal thin layer of a-SnO_2, c-SnO_2, or NC-SnO_2. Top-view SEM images of the perovskite films deposited on the different EELs are shown in Figure S2. As seen, the grain size of perovskite film on a-SnO_2 is slightly larger than perovskite films on top of the bare mp-TiO_2 scaffold or NC-SnO_2. This indicates that the number of nucleation cites in amorphous SnO_2 (continuous film) is less than other substrates, resulting in larger grain size for perovskite film.

X-ray diffraction (XRD) patterns of SnO_2 films deposited from solution and the NC-colloid are shown in Figure 1a. The data show the spin-coated SnO_2 film annealed at 180 °C to be amorphous turning fully crystalline upon annealing at 450 °C.[32] The reflections match the known pattern of tetragonal SnO_2 (JCPDS Card No: 41-1445). The NC-SnO_2 layer shows similar XRD reflections although it exhibits a stronger prevalence of (101) over the (110) and (200) facets. It was deposited onto the mp-TiO_2 scaffold by spin coating of a colloidal solution of SnO_2 nanocrystals with a 3-5 nm particle size (Figure S3), followed by annealing at 150 °C.[33]

Figure 1b,c demonstrate the optical properties of the triple cation perovskite films deposited on the different EELs. Panel (b) shows the absorption onset and luminescence peak to be around 770 nm, corresponding to a band gap of 1.61 eV. The photoluminence (PL) decay is significantly influenced by the nature of the EEL reflecting its effectiveness in scavenging photo-generated conduction band electrons from the perovskite light harvesters (Figure 1c). The PL lifetimes obtained from exponential fits of the decay curves are 2.43 ns, 3.21 ns, and 1.93 ns for mp-TiO_2, mp-TiO_2/NC-SnO_2, and mp-TiO_2/a-SnO_2, respectively, showing that the amorphous SnO_2 extracts electrons more rapidly from the pervoskite than the bare TiO_2 scaffold while the SnO_2-NC show a slower rate.

Table 1. Photovoltaic metrics for best performing devices based on mp-TiO_2, mp-TiO_2/SnO_2-NCs, and mp-TiO_2/a-SnO_2 with different scan directions

Sample	V_{oc}(V)	J_{sc}(mA/cm^2)	*FF* (%)	PCE (%)	Hysteresis index (%)
Mp-TiO_2-forward	1.078	22.12	78.1	18.62	2.7
Mp-TiO_2-backward	1.098	22.21	78.5	19.14	
Mp-TiO_2/SnO_2-NCs-forward	1.114	21.76	67.8	16.43	3
Mp-TiO_2-SnO_2-NCs-backward	1.135	21.83	68.4	16.95	
Mp-TiO_2/a-SnO_2-forward	1.171	22.47	76.8	20.21	1.1
Mp-TiO_2/a-SnO_2-backward	1.168	22.51	77.6	20.4	

We fabricated perovskite solar cells endowed with these EELs as explained in the experimental section. Figure 2a presents the cross-sectional SEM image of a PSC based on mp-TiO_2/a-SnO_2. Current density-voltage (*J-V)* curves of devices employing the three different EELs under

simulated (AM1.5G) solar irradiation are shown in Figure 2b for both backward and forward scanning directions. The PV metrics for best performing devices are listed in Table1 and *J-V* curves are shown in Figure 2b. The PSC based on mp-TiO_2/a-SnO_2 presents the highest PCE of 20.4% with a V_{oc} of 1.168 V, J_{sc} of 22.51, and *FF* of 77.6%, clearly outperforming the bare and mp-TiO_2/NC- SnO_2 films. The reference cell using bare mp-TiO_2 gave a J_{sc} of 22.21 mA/cm^2, V_{oc} of 1.098 V, fill factor (*FF*) of 78.5%, and PCE of 19.14%.

Note, the high V_{oc} of 1.17 V obtained with mp-TiO_2/a-SnO_2 as EEL exceeding that of the bare TiO_2 reference by 80-100 mV. This finding is counterintuitive as one would expect SnO_2 to produce a lower V_{oc} than TiO_2 (anatase) due to the 0.3 eV larger offset of its conduction band edge energy with respect to that of the perovskite. In keeping with this expectation, Dai et. al. [34] obtained a V_{oc} of only 0.7 V with a PSC employing meosporous SnO_2 (mp-SnO_2) instead of TiO_2 as electron extracting scaffold. Upon covering the mp-SnO_2 film with a thin layer of TiO_2 the V_{oc} improved to 0.93 V. Strikingly, we observe exactly the opposite behavior, *i.e.* by coating the mp-TiO_2 scaffold with a thin layer of a-SnO_2, we greatly improve the V_{oc} pushing it near 1.2 V. In order to rationalize these seemingly contradictory findings, we draw attention to our recent discovery[35] that the conduction band edge energy of amorphous SnO_2 is lifted by about 0.5 eV with respect to that of the tetragonal crystalline phase. This shift improves the band alignment with the perovskite allowing for rapid carrier extraction without voltage loss. The amorphous overlayer shows also the lowest hysteresis index, *i.e.* 1.1 % calculated from the formula $h=(PCE_{backward}- PCE_{forward})/PCE_{backward})*100$. This again confirms that electrons are extracted rapidly without undergoing significant trapping at the perovskite/EEL interface.

Figure S4 demonstrates statistical data for batches of 15 PSCs for each of the three EELs. The average values of photovoltaic metrics confirm that the amorphous SnO_2 film coating on mp-

TiO_2 increases all photovoltaic parameters except *FF*. In particular, the V_{oc} of device using mp-TiO_2/a-SnO_2 is greatly increased. However, the presence of SnO_2-NCs on mp-TiO_2 decreases the J_{sc} and especially *FF* with respect to the reference cell. This indicates that the crystal structure of the SnO_2 film plays a key role in device performance.[35] Figure S5 shows the *J-V* curve of a PSC using the SnO_2 film on mp-TiO_2 annealed at 450 °C. The results prove that the conduction band edge of crystalline SnO_2 film (as shown in Figure 1a) is much less favorably aligned with the perovskite layer than that of the amorphous form resulting in a poorer device performance. In case of crystalline SnO_2 films (SnO_2-NCs or SnO_2 annealed at 450 °C), despite similarity of their XRD features, the PV performance of the crystalline SnO_2-annealed at 450°C is worse than that of the SnO_2-NCs, which can be attributed to quantum confinement effects in the SnO_2 nanocrystals,[36] changing the band alignment of EEL with respect to perovskite (Figure 3b).

Figure 2c shows the stabilized maximum power delivered from mp-TiO_2, mp-TiO_2/SnO_2-NCs, and mp-TiO_2/a-SnO_2 PSCs to be18.89, 16.75, and 20.27 mW/cm^2, respectively, in line with the PCE values derived from the *J-V* curves. Figure 2d depicts the wavelength dependence of the external quantum efficiency (EQE) of these devices. The EQE values of the perovskite device on mp-TiO_2/a-SnO_2 are slightly higher than those of others cell, which is in good agreement with the observed trends in the photocurrent.

In order to rationalize the effect of the SnO_2 structure on the photovoltaic performance, we derived the band alignment of the perovskite with the EELs from ultraviolet photoelectron spectroscopy (UPS) and UV-vis absorption measurements. Figure 3a shows the valence band and Fermi level of the EELs calculated from the UPS data. The valence band edges of mp-TiO_2, SnO_2-NCs, and a-SnO_2 films are positioned at 7.92 eV, 8.22 eV, and 8.44 eV below vacuum, respectively. From the UV-visible data shown in Figure 3b, the band gaps of mp-TiO_2, SnO_2-

NCs, and a-SnO_2 are 3.3 eV, 4.05 eV, and 4.1 eV, respectively. We used these values to derive the energy band diagrams plotted in Figure 3 for devices employing mp-TiO_2, mp-TiO_2/SnO_2-NCs, and mp-TiO_2/a-SnO_2 as EELs. Clearly, the conduction band edge of a-SnO_2 on mp-TiO_2 is optimally positioned to facilitate the extraction of electrons from the perovskite and their subsequent injection into the TiO_2 scaffold, while the nano-crystalline layer of SnO_2 acts as a barrier explaining the poor fill factors produced with this architecture. The conduction band edge for the bare mp-TiO_2 scaffold is at 0.4 eV lower energy than that of the perovskite accounting for the observed decrease in V_{oc} to an average of 1.08 V. This offset is greatly enhanced for the c-SnO_2 overlayer, reducing the V_{oc} substantially to below 1 V.

Figure 6S shows results from intensity modulated photovoltage spectroscopy (IMVS) measurements carried our at different open circuit voltages, which were adjusted by varying the light intensity. The derived time constants in panel are in the 10–100 microsecond domain and are attributed to carrier recombination. These recombination times are of similar magnitude for the two investigated types of PSCs using EELs with and without a-SnO_2 overlayers on the mp-TiO_2 scaffold. Nevertheless, the values for bare mp-TiO_2 show steeper voltage dependence than the ones obtained with a-SnO_2/mp-TiO_2 double layer. The two curves reach a crossing point at ca 0.98 V beyond, which the carriers recombine more slowly for the a-SnO_2 covered than for the bare TiO_2 films.

However the IMVS spectra shown in panel 4b reveal the presence of a second time constant for the mp-TiO_2 sample which is much less pronounced for the mp-TiO_2/a-SnO_2 one. In fact, each peak of the imaginary part of IMVS spectra can be associated to a time constant of the device under investigation. This feature is attributed to the recombination of carriers being trapped in deep states slowing down the time constants to the hundred millisecond domain. This slow

relaxation process may also be couple to the displacement of ions in the local space charge electric field generated by the trapped carriers.

Even though we can observe a small peak also in the spectra of the double layer sample mp-TiO_2/a-SnO_2, it appears significantly reduced in magnitude and is evident only for very low illumination intensities. This shows that the amorphous SnO_2 layer is capable of mitigate the deleterious effect of electron trapping states at the interface between the pervoskite layer and the TiO_2.

Moreover, the direct comparison of electroluminescence measurements confirmed the capability of the a-SnO_2 treatment in suppressing the nonradiative recombination losses (Figure 4). In fact, the external quantum efficiency (EQE) of mp-TiO_2/a-SnO_2 sample at the same current density (16 mA/cm^2) is higher than the standard mp-TiO_2 structure, reaching approximately 0.5% in line with the higher V_{oc} values observed for the sample with a-SnO_2 as EEL. Note that this value is comparable with the state of the art values.

Due to the photocatalytic action of TiO_2 based-perovskite solar cells, TiO_2 EEL is prone to degradation under UV light. Eliminating this unwanted effect is important for large scale outdoor application of PSCs. Encouragingly, we observed that the device based on mp-TiO_2/a-SnO_2 is more stable than mp-TiO_2 based solar cell under continuous UV light. For this experiment, the devices were exposed to UV light and measured after each 3 hours. Figure 5 shows the UV stability of devices on mp-TiO_2 and mp-TiO_2/a-SnO_2 after 60 hours exposure to UV lamp. The PCE of perovskite solar cell based on mp-TiO_2/a-SnO_2 is maintained almost 97% of its initial value, while bare TiO_2 shows 18% PCE loss under this condition. This clearly shows another advantage of our proposed double layers EEL for perovskite solar cell.

Conclusions

Our results show that applying a thin amorphous overlayer of SnO_2 on mesoporous TiO_2 scaffold improves not only the power conversion efficiency of perovskite solar cells but also enhances the UV stability of the device. The strong gain in the V_{oc} enabled by the amorphous SnO_2 capping layer stands in stark contrast to the dramatic losses in the V_{oc} and PCE encountered with crystalline SnO_2 films. This striking difference arises from larger band gap of amorphous layer and better band alignment with respect to triple cation perovskite compared to crystalline SnO_2. Based on mp-TiO_2/a-SnO_2 architecture, a perovskite solar cell with PCE of 20.4% was achieved, which is 6% higher than bare mp-TiO_2 device. Moreover, it was discovered that the UV stability of perovskite device for double layer mp-TiO_2/a-SnO_2 is improved drastically compared with pure mp-TiO_2 ETL, where after 60 h exposure to UV lamp, the PCE loss in only 3%.

Associated content

Supporting Information

The Supporting Information is available free of charge on the ACS Publications website.

Author information

Corresponding Author

*E-mail: michael.graetzel@epfl.ch

Notes

The authors declare no competing financial interest.

Acknowledgments

M.G. and S.M.Z. are grateful for the Graphene Flagship Core1under grant agreement 696656 and the King Abdulaziz City for Science and Technology (KACST) for financial support.

M.M.T. wants to thank school engineering, hong kong university of science and technology (HKUST).

References

[1] Lee, J. W.; Kim, H. S.; Park, N. G. *Acc. Chem. Res.* **2016***, 49* (2), 311-319.

[2] Yang, W. S.; Park, B. W.; Jung, E. H.; Jeon, N. J.; Kim, Y. C.; Lee, D. U.; Shin, S. S.; Seo, J.; Kim, E. K.; Noh, J. H.; Seok, S. I. *Science* **2017**, *356* (6345), 1376-1379.

[3] Grätzel, M. *Nat. Mater.* **2014**, *13* (9), 838-842.

[4] Liu, M.; Johnston, M. B.; Snaith, H. J. *Nature* **2013**, *501*(7467), 395-398.

[5] Ng, A.; Ren, Z.; Shen, Q.; Cheung, S. H.; Gokkaya, H. C.; So, S. K.; Djurišić, A. B.; Wan, Y.; Wu, X.; Surya, C. *ACS Appl. Mater. Interfaces* **2016**, *8* (48), 32805-32814.

[6] Tavakoli, M. M.; Tavakoli, R.; Hasanzadeh, S.; Mirfasih, M. H. *J. Phys. Chem. C* **2016**, *120* (35), 19531-19536.

[7] Li, T.; Pan, Y.; Wang, Z.; Xia, Y.; Chen, Y.; Huang, W. *J. Mater. Chem. A* **2017**, *5* (25), 12602-12652.

[8] Jeon, N. J.; Noh, J. H.; Yang, W. S.; Kim, Y. C.; Ryu, S.; Seo, J.; Seok, S. I. *Nature* **2015**, *517* (7535), 476-480.

[9] Jeon, N. J.; Noh, J. H.; Kim, Y. C.; Yang, W. S.; Ryu, S.; Seok, S. I. *Nat. Mater.* **2014***, 13* (9), 897-903.

[10] Xiao, M.; Huang, F.; Huang, W.; Dkhissi, Y.; Zhu, Y.; Etheridge, J.,; Gray-Weale, A.; Bach, U.; Cheng, Y. B.; Spiccia, L. *Angewandte Chemie* **2014**, *126* (37),10056-10061.

[11] Nie, W.; Tsai, H.; Asadpour, R.; Blancon, J. C.; Neukirch, A. J.; Gupta, G.; Crochet, J. J.; Chhowalla, M.; Tretiak, S.; Alam, M. A.; Wang, H. L. *Science* **2015**, *347* (6221), 522-525.

[12] Liang, P. W.; Liao, C. Y.; Chueh, C. C.; Zuo, F.; Williams, S. T.; Xin, X. K.; Lin, J.; Jen, A. K. Y. *Adv. Mater.* **2014***, 26* (22), 3748-3754.

[13] Burschka, J.; Pellet, N.,; Moon, S. J.; Humphry-Baker, R.; Gao, P.; Nazeeruddin, M. K.; Grätzel, M. *Nature* **2013**, *499* (7458), 316-319.

[14] Tavakoli, M. M.; Tavakoli, R.; Nourbakhsh, Z.; Waleed, A.; Virk, U. S.; Fan, Z. *Adv. Mater. Interfaces* **2016**, *3* (11),1500790.

[15] Lee, Y. H.; Paek, S.; Cho, K. T.; Oveisi, E.; Gao, P.; Lee, S. H.; Park, J. S.; Zhang, Y.; Humphry-Baker, R.; Asiri, A. M.; Nazeeruddin, M. K. *J. Mater. Chem. A* **2017**, *5* (25), 12729-12734.

[16] Giordano, F.; Abate, A.; Baena, J. P. C.; Saliba, M.; Matsui, T.; Im, S. H.; Zakeeruddin, S. M.; Nazeeruddin, M. K.; Hagfeldt, A.; Graetzel, M. *Nat. Commun.* **2016**, *7*, 10379.

[17] Leijtens, T.; Eperon, G. E.; Pathak, S.; Abate, A.; Lee, M. M.; Snaith, H. J. *Nat. Commun.* **2013**, *4*, 2885.

[18] Niu, G.; Guo, X.; Wang, L. *J. Mater. Chem. A* **2015**, *3* (17), 8970-8980.

[19] Baena, J. P. C.; Steier, L.; Tress, W.; Saliba, M.; Neutzner, S.; Matsui, T.; Giordano, F.; Jacobsson, T. J.; Kandada, A. R. S.; Zakeeruddin, S. M.; Petrozza, A. *Energy Environ. Sci.* **2016**, *8* (10), 2928-2934.

[20] Anaraki, E.H.; Kermanpur, A.; Steier, L.; Domanski, K.; Matsui, T.; Tress, W.; Saliba, M.; Abate, A.; Grätzel, M.; Hagfeldt, A.; Correa-Baena, J. P. *Energy Environ. Sci.* **2016***, 9* (10), 3128-3134.

[21] Dong, Q.; Xue, Y.; Wang, S.; Wang, L.; Chen, F.; Zhang, S.; Chi, R.; Zhao, L.; Shi. Y. *Sci. China Mater.* **2017**, *60* (10), 963-976.

[22] Minami, T.; Nanto, H.; Takata, S. *Japanese journal of applied physics* **1988**, *27* (3A), L287.

[23] Jung, K. H.; Seo, J. Y.; Lee, S.; Shin, H.; Park, N. G. *J. Mater. Chem. A* **2017**, *5* (47)**,** 24790-24803.

[24] Chen, H.; Liu, D.; Wang, Y.; Wang, C.; Zhang, T.; Zhang, P.; Sarvari, H.; Chen, Z.; Li, S. *Nanoscale Research Lett.* **2017**, *12* (1), 238.

[25] Ren, X.; Yang, D.; Yang, Z.; Feng, J.; Zhu, X.; Niu, J.; Liu, Y.; Zhao, W.; Liu, S. F. *ACS Appl. Mater. Interfaces* **2017**, *9* (3), 2421-2429.

[26] Jiang, Q.; Chu, Z.; Wang, P.; Yang, X.; Liu, H.; Wang, Y.; Yin, Z.; Wu, J.; Zhang, X.; You, J. *Adv. Mater.* **2017**, *29* (46), 1703852.

[27] Song, S.; Kang, G.; Pyeon, L.; Lim, C.; Lee, G. Y.; Park, T.; Choi, J.; Systematically Optimized Bilayered Electron Transport Layer for Highly Efficient Planar Perovskite Solar Cells (η= 21.1%). *ACS Energy Lett*. **2017**, *2* (12), 2667-2673.

[28] Dong, Q.; Shi, Y.; Wang, K.; Li, Y.; Wang, S.; Zhang, H.; Xing, Y.; Du, Y.; Bai, X.; Ma, T. *J. Phys. Chem. C* **2015***, 119* (19), 10212-10217.

[29] Wang, H.; Sayeed, M. A.; Wang, T. *Australian Journal of Chemistry* **2015**, *68* (11), 1783-1788.

[30] Bai, Y.; Fang, Y.; Deng, Y.; Wang, Q.; Zhao, J.; Zheng, X.; Zhang, Y.; Huang, J. *Chem. Sus. Chem.* **2016**, *9* (18), 2686-2691.

[31] Ko, Y.; Kim, Y. R.; Jang, H.; Lee, C.; Kang, M. G.; Jun, Y. *Nanoscale Research Lett.* **2017**, *12* (1), 498.

[32] Mohamedi, M.; Lee, S. J.; Takahashi, D.; Nishizawa, M.; Itoh, T.; Uchida, I. *Electrochim. Acta* **2001**, *46* (8), 1161-1168.

[33] Jiang, Q.; Zhang, L.; Wang, H.; Yang, X.; Meng, J.; Liu, H.; Yin, Z.; Wu, J.; Zhang, X.; You, J. *Nat. Energy* **2016**, *2*, 16177-16183.

[34] Li, Y.; Zhu, J.; Huang, Y.; Liu, F.; Lv, M.; Chen, S.; Hu, L.; Tang, J.; Yao, J.; Dai, S. *RSC Adv.* **2015**, *5* (36), 28424-28429.

[35] Kavan, L.; Steier, L.; Grätzel, M. *J. Phys. Chem. C* **2016**, *121* (1), 342-350.

[36] Deng, H. X.; Li, S. S.; Li, J. *J. Phys. Chem. C* **2010**, *114* (11), 4841-4845.

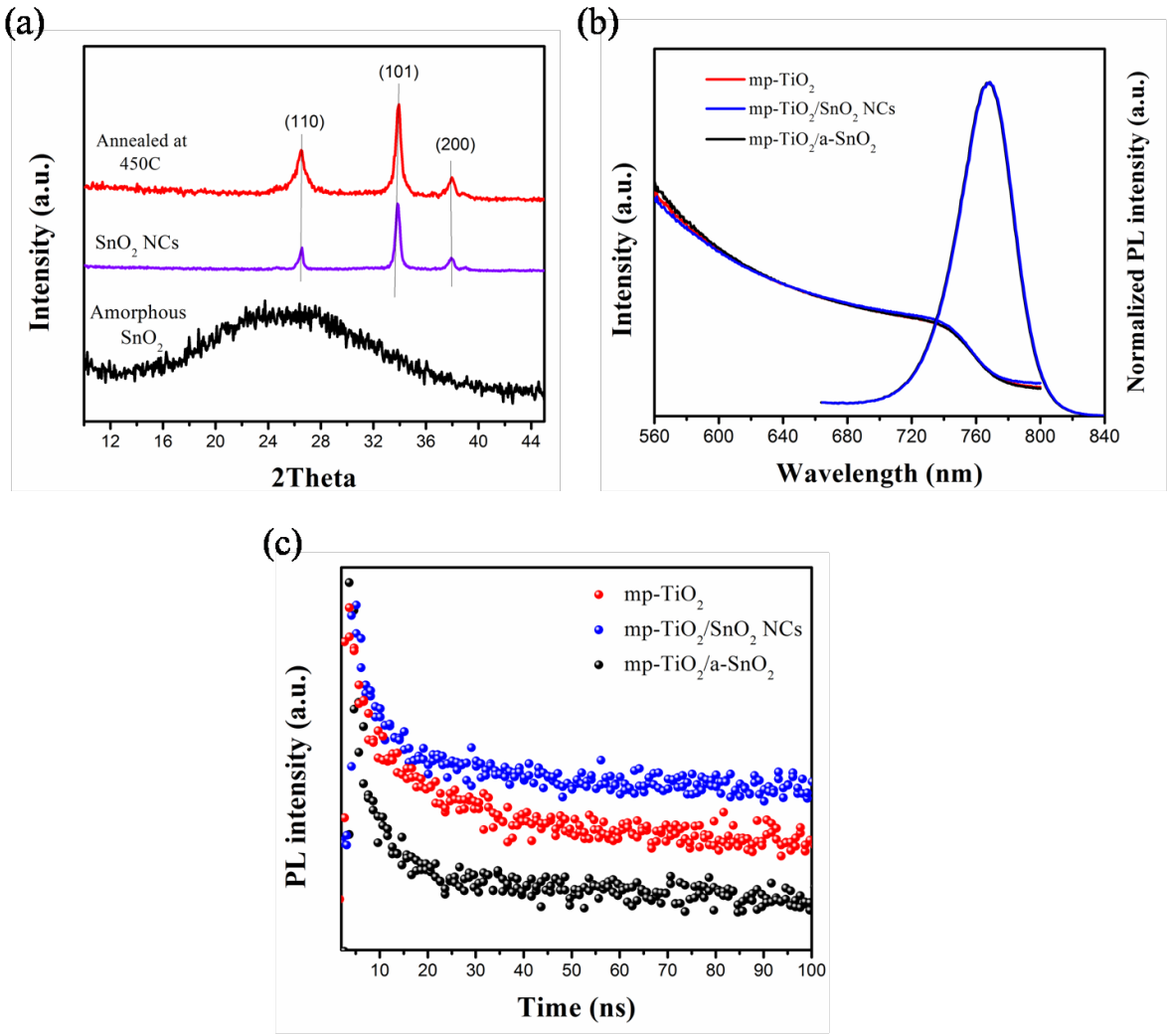

Figure 1. XRD patterns of SnO_2 films annealed at 180 °C (amorphous phase) and 450 °C (crystalline phase) and SnO_2-NCs layer annealed at 150 °C. For this experiment the SnO_2 films were deposited on a silicon support. (b) UV-visible absorption and photoluminescence (PL) spectra of the triple cation pervoskite and (c) time-resolved PL (TRPL) curves of perovskite films on mp-TiO_2, mp-TiO_2/SnO_2-NCs, and mp-TiO_2/a-SnO_2.

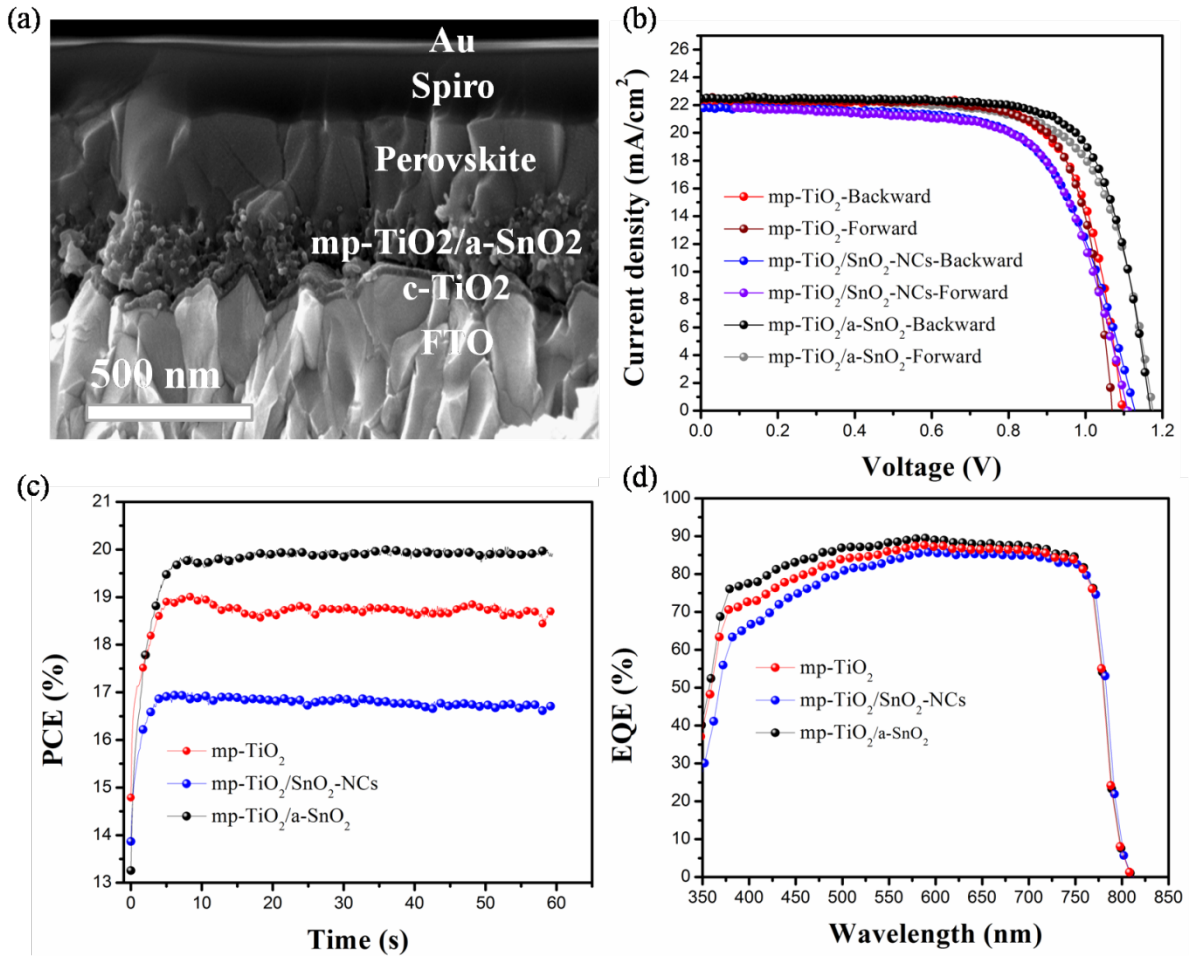

Figure 2. (a) Cross-sectional SEM image of perovskite solar cell based on mp-TiO_2/a-SnO_2. (b) *J-V* curves, (c) Maximum power point tracking (MPPT), and (d) EQE spectra of PSCs based on mp-TiO_2, mp-TiO_2/SnO_2-NCs, and mp-TiO_2/a-SnO_2.

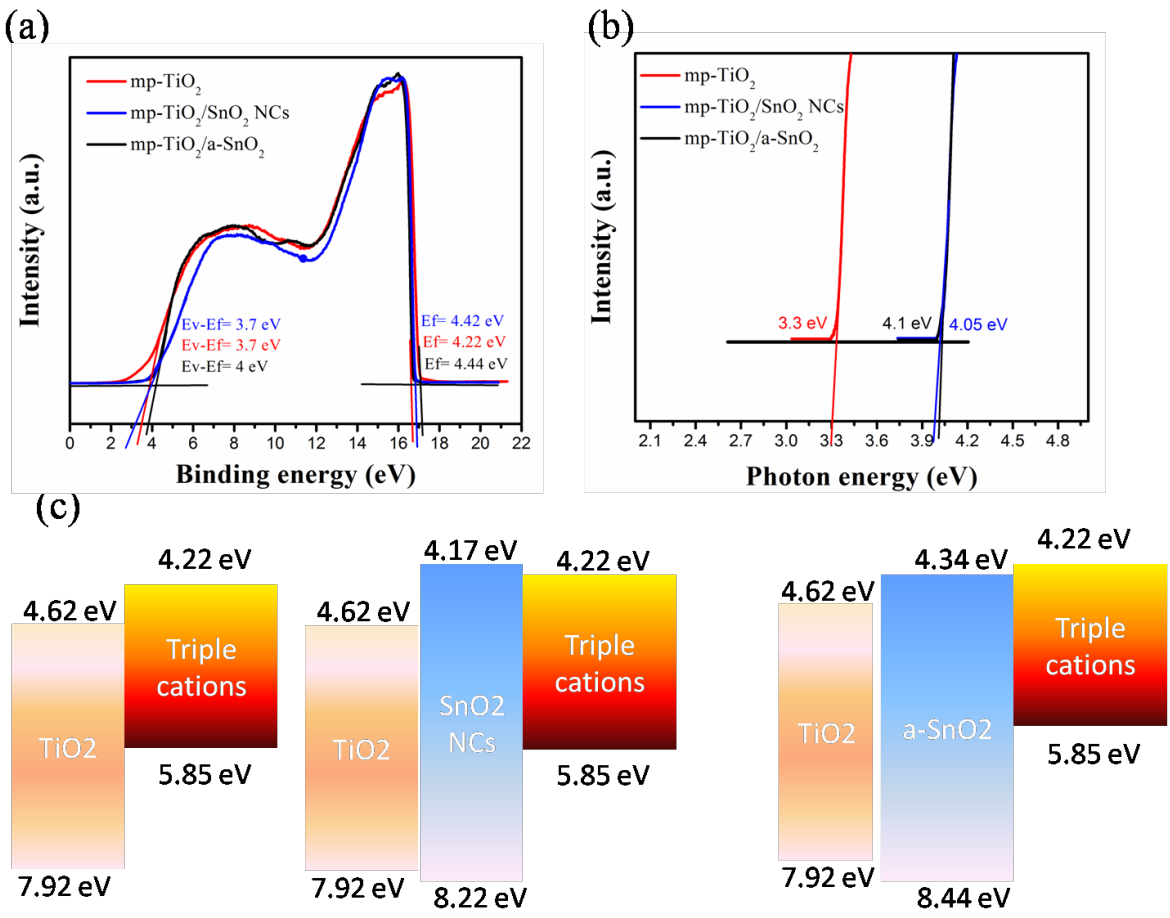

Figure 3. (a) UPS measurements and (b) UV-visible spectra of SnO_2 and TiO_2 films on Si substrate for band levels calculation. (b) Schematics of band alignment for devices based on mp-TiO_2, mp-TiO_2/SnO2-NCs, and mp-TiO_2/a-SnO_2.

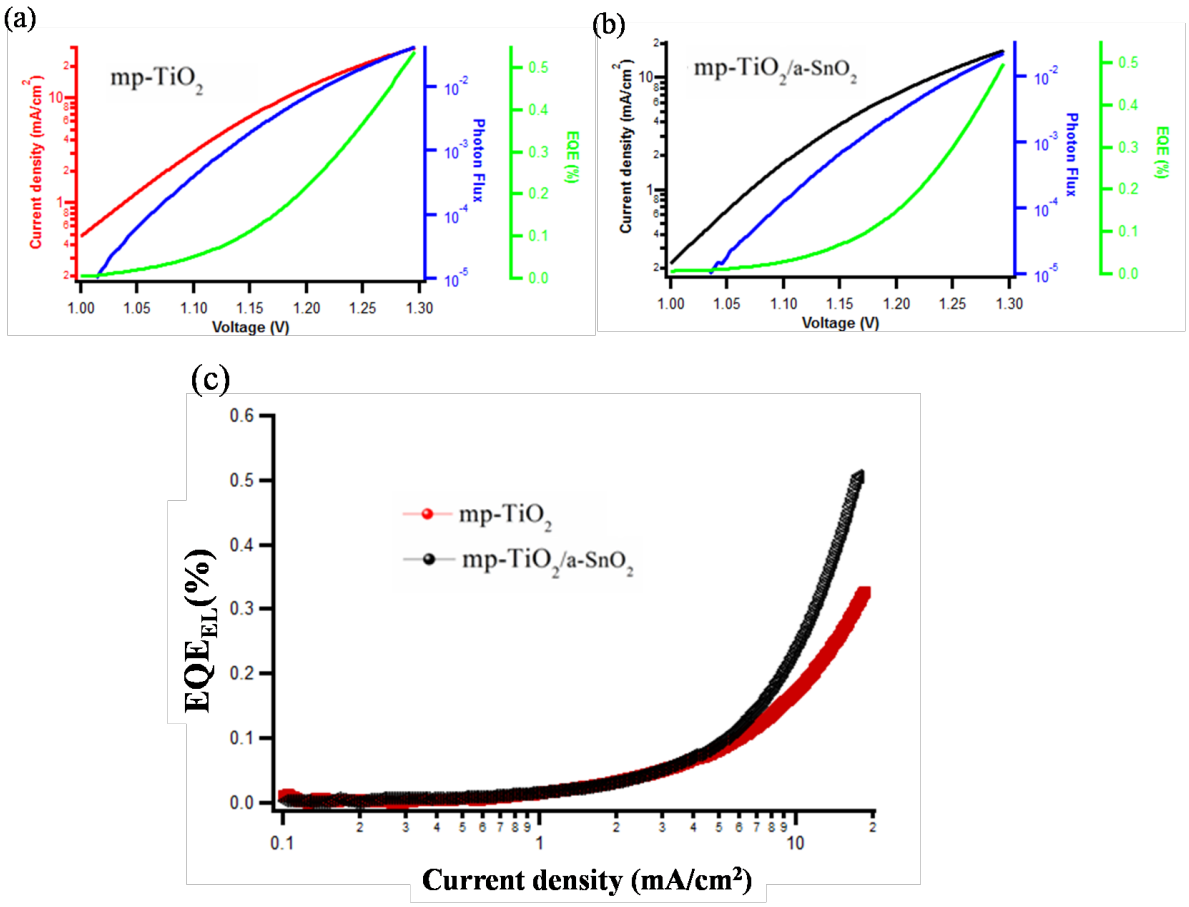

Figure 4. Dark current (black) photon flux (blue) and external quantum efficiency (EQE) (green) measurements for devices on mp-TiO_2 (a) and mp-TiO_2/a-SnO_2 ETL (b). (c) Comparison of EQE at the same dark current for mp-TiO_2 (red) and mp-TiO_2/a-SnO_2 ETL (black). Note that the device area in this test was ~ 0.25 cm^2.

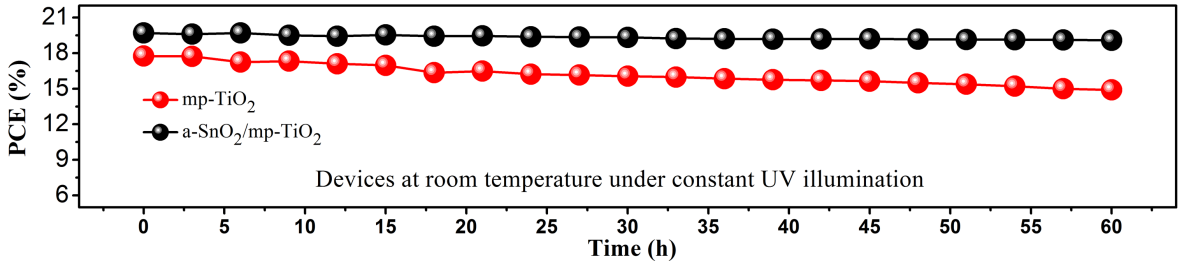

Figure 5. UV stability of perovskite solar cells based on mp-TiO_2 and mp-TiO_2-a-SnO_2 EELs at room temperature inside a dry air box.

Supporting Information

Mesoscopic Oxide Double Layer as Electron Specific Contact for Highly Efficient and UV Stable Perovskite Photovoltaics

Mohammad Mahdi Tavakoli[1,2], Fabrizio Giordano[1], Shaik Mohammed Zakeeruddin[1], Michael Grätzel[1]*

[1]*Institut des Sciences et Ingénierie Chimiques, Ecole Polytechnique Fédérale de Lausanne (EPFL), EPFL–BCH, CH–1015 Lausanne, Switzerland*

[2]*Department of Materials Science and Engineering, Sharif University of Technology, 14588 Tehran, Iran*

* Corresponding author: michael.graetzel@epfl.ch

Experimental section

Device fabrication:

FTO glasses (NSG-10) were chemically etched using zinc powder and HCl solution (2 M), followed by four steps ultrasonic cleaning using Triton X100 (1 vol% in deionized water), DI water, acetone, and ethanol, respectively. All substrates were further cleaned by ozone plasma for 15 min, before deposition of each EEL. To prepare TiO_2 compact layer, a precursor solution of titanium diisopropoxide (Sigma-Aldrich) in ethanol was deposited on the substrates at 450 °C using spray pyrolysis process, followed by 30 min annealing at 450°C. Thereafter, a 150 nm-thick mesoporous TiO_2 was spin coated on compact TiO_2 (4000 rpm for 15 s with a ramp rate of 2000 rpm/s) from a diluted TiO_2 paste (Dyesol 30 NR-D) in ethanol, followed by annealing the substrates at 450°C for 30 min. To modify the surface of mp-TiO_2, SnO_2 precursor solution (0.1 M $SnCl_2.2H_2O$ in ethanol) was spin-coated on top of mp-TiO_2 with a 20 s delay time to allow for full impregnation before spinning at 6000 rpm for 40 s. Subsequently , the film was annealed at 180 °C for 1 hour. We converted the a–SnO_2 to crystalline phase (c-SnO_2) by annealing the film at 450 °C for 1 hour. The SnO_2 quantum dots (NC-SnO_2) had a size of 3-5 nm and were deposited on top of the mp-TiO_2 by spin coating at 5000 rpm for 20 s with 2000 rpm/s ramp-rate, followed by annealing at 150 °C for 1 hour.

For deposition of perovskite film a precursor solution of $(FAPbI_3)_{0.87}(MAPbBr_3)_{0.13}$ was first prepared by mixing FAI (1.05 M, Dyesol), PbI_2 (1.10 M, TCI), MABr (0.185 M, Dyesol) and $PbBr_2$ (0.185 M, TCI) in a mixed solvent of DMF:DMSO = 4:1 (volume ratio). Then, a 5 vol% of 1.5 M CsI solution in DMSO was added into the perovskite solution in order to have a triple cation perovskite. The solution was spin-coated at 1000 rpm for 10 s and, continuously at 4000 rpm for 30 s. During the second phase, 200 μL of chlorobenzene was dropped on top film 10

second before end of spinning. Thereafter, the film was annealed first at 120 °C for 10 min followed by 40 min at 100 °C. After annealing and cooling the samples, spiro-OMeTAD solution in chlorobenzene (70 mM) containing a solution bis(trifluoromethylsulfonyl)imide lithium salt (Li-TFSI, Sigma-Aldrich) in acetonitrile (200 mg/400 μL) and (4-tert-butylpyridine-Sigma-Aldrich) with molar ratios of 0.5 and 3.3, respectively, was prepared and spin-coated at 4000 rpm for 20 s (using a ramp rate of 2000 rpm/s). Finally, 80-nm thick gold was thermally evaporated as a back contact to complete the device structure with a masked active area of 0.16 cm^2.

Film characterization

The morphology of perovskite film and device structure were studied using a ZEISS Merlin high resolution Scanning electron microscopy (HRSEM). The quality and crystal structure of perovskite films were characterized by using X-ray diffraction (Bruker D8 X-ray Diffractometer, USA) utilizing a Cu *Kα*-radiation. Transmission electron microscopy (JEOL (2010F) under an accelerating voltage of 200 volts) was employed to take images from SnO_2 nanocrystals.

For optical absorption measurement, a Varian Carry 500 spectrometer (Varian, USA) was used. To record steady-state photoluminescence spectra, an Edinburgh Instruments FLS920P fluorescence spectrometer. For time resolved measurements (TRPL), we employed a picosecond pulsed diode laser (EPL-405, excitation wavelength 405 nm, pulse width 49 ps) was PL decay curves were fitted to the exponential function: $I(t) = I_0 \exp(-(t_i/\tau_i)^{\beta i})$, where τ_i is the decay lifetime and β_i is a stretching parameter.

Device characterization

The solar cells were measured under AM1.5G sun simulator (a 450 W Xenon lamp (Oriel), with intensity of 100 $mWcm^{-2}$, equipped with a Schott K113 Tempax sunlight filter (Praezisions Glas&Optik GmbH) to simulate the emission spectra of AM1.5G standard in the region of 350-

750 nm. Calibration of the lamp was performed using standard Silicon solar cell (KG5-filtered Si reference cell). To measure the current density-voltage (*J-V*) curves, a 2400 series source meter (Keithley, USA) instrument was employed. The voltage range for *J-V* sweeps was between 0 and 1.2 V, with a step increment of 0.005 V and a delay time of 200 ms at each point. External quantum efficiency (EQE) spectra were measured with a commercial apparatus (Arkeo-Ariadne, Cicci Research s.r.l.) based on a 300 Watts Xenon lamp.

Electroluminescence and IMVS measurements. The photon flux emitted by the perovskite solar cells was detected with a 1cm^2 Silicon Photodiode (Hamamatsu s1227-1010BQ). The bias to the device under test was provided by a Bio-Logic SP300 potentiostat, which was used to measure also the short circuit current of the photodetector on another channel. IMVS measurements were performed by Bio-Logic SP300 in combination withthe Galvano Staircase Spectroscopy routine from EC-Lab Software.

The UV stability of devices was measured inside a dry air box using a UV lamp (Spectronics ENF-240C) with power of 40 mW/cm^2.

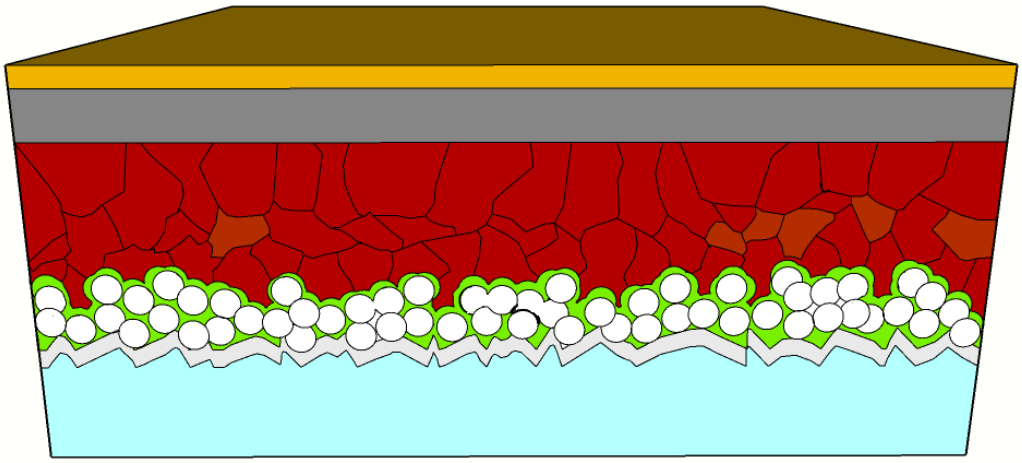

Figure S1. Schematic cross sectional image of the investigated PSC architecture. The blue bottom layer of the stack denotes the TCO glass, covered by blocking layer of TiO_2 (brown). The interconnected white nanoparticles of the TiO_2 scaffold are coated with a conformal layer (green) of either amorphous, crystalline or nanocrystalline SnO_2. The pervoskite light harvesting layer indicated in brown-red color is covered with the gray HTL and the gold contact.

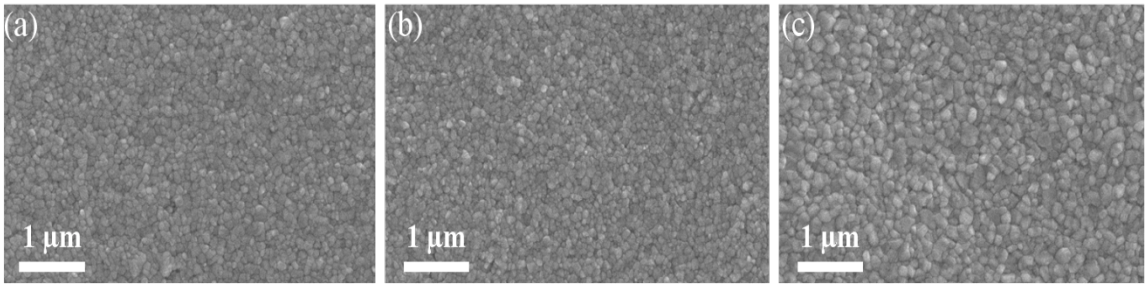

Figure S2. Top-view SEM images of perovskite film deposited on mp-TiO_2 (a), mp-TiO_2/SnO_2-NCs (b), and mp-TiO_2/a-SnO_2 (c).

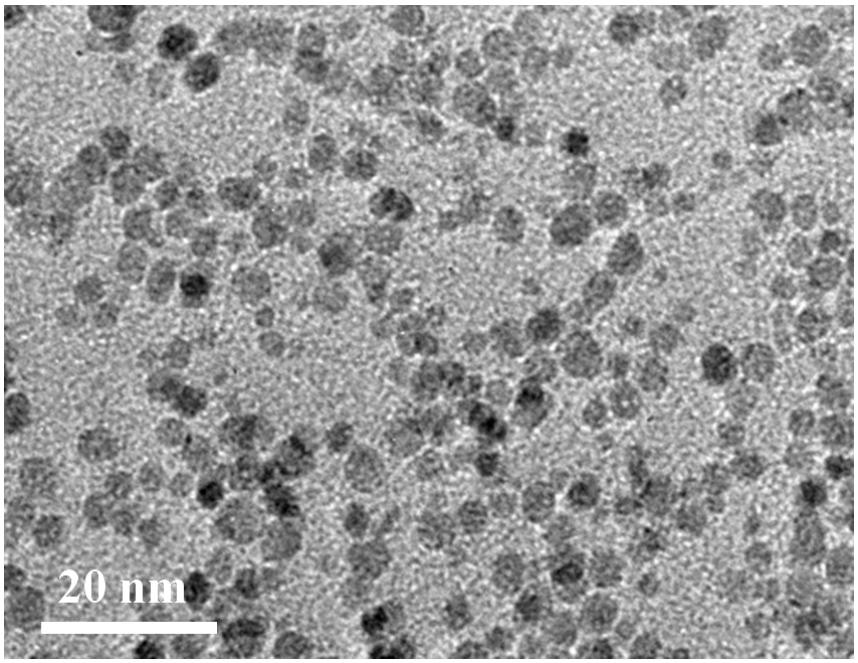

Figure S3. TEM image of commercial SnO_2 nanocrystals with average size of 3-5 nm.

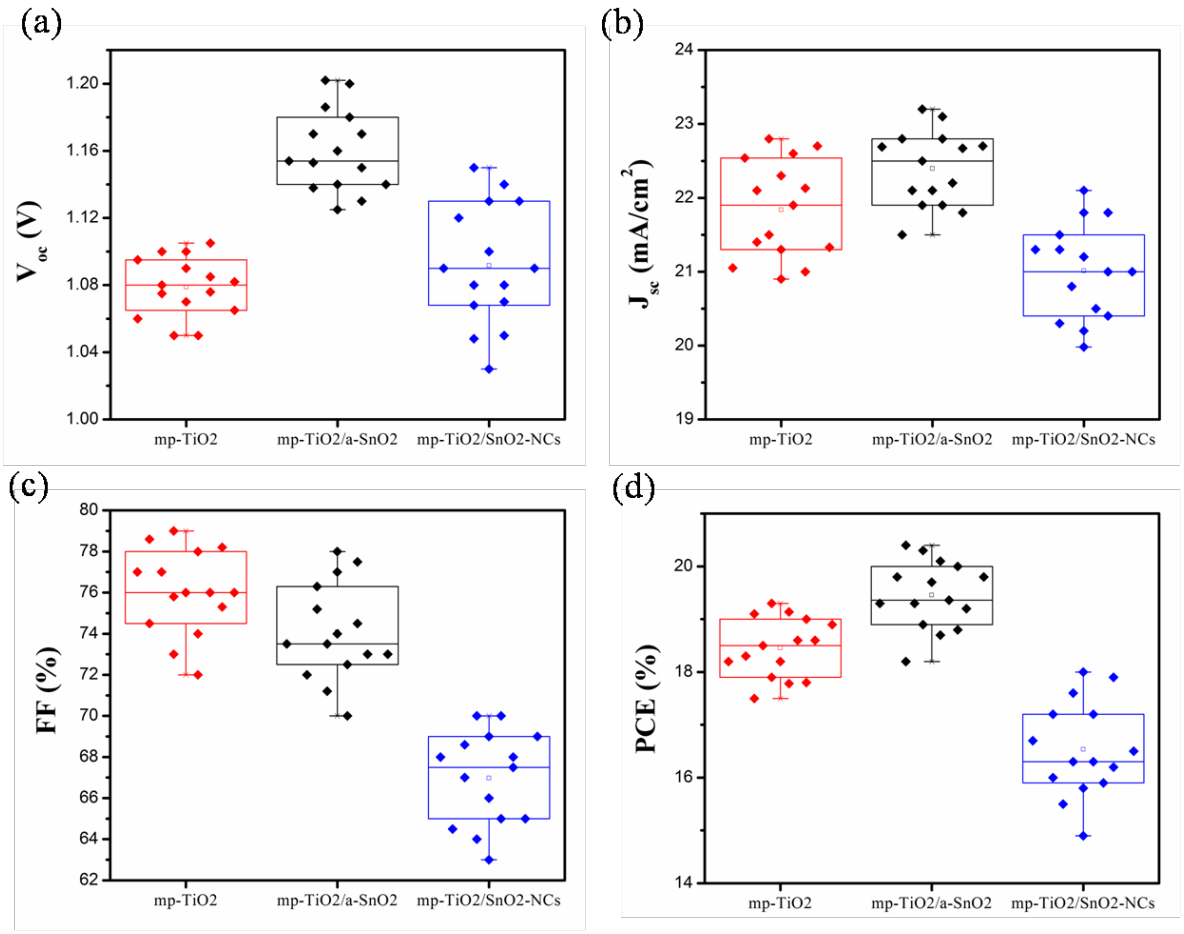

Figure S4. Statistical photovoltaic data for perovskite solar cells based on mp-TiO_2, mp-TiO_2/SnO_2-NC, and mp-TiO_2/a-SnO_2.

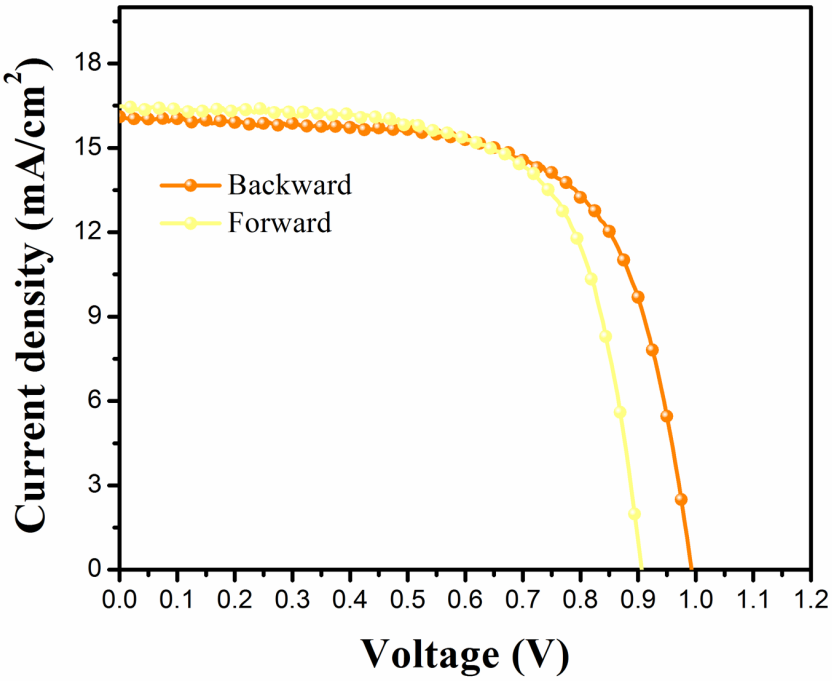

Figure S5. *J-V* curve of perovskite solar cells based on mp-TiO_2/crystalline SnO_2 annealed at 450 °C for 1 hour with forward and backward scan directions.

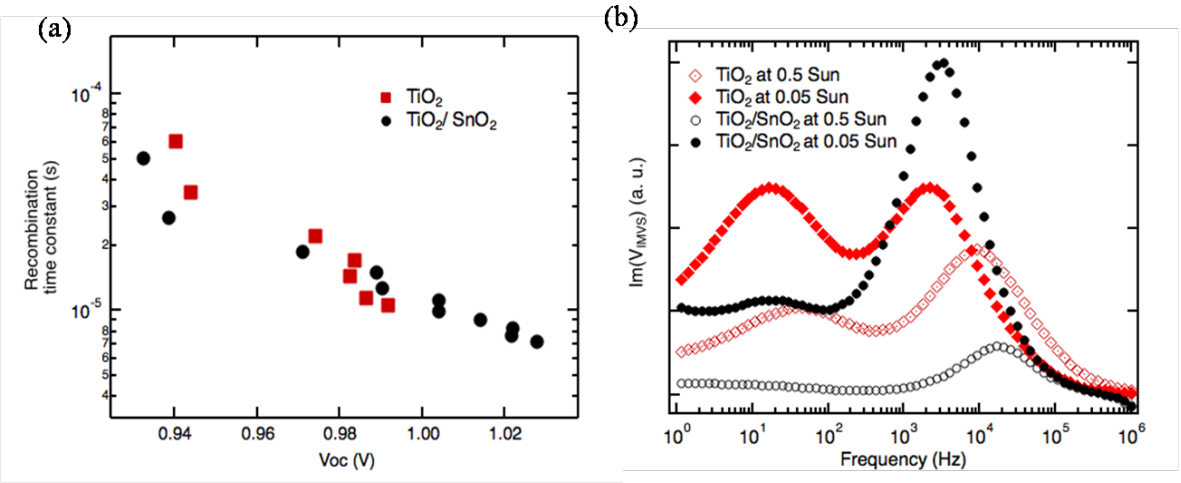

Figure S6. (a) Recombination time constants for mp-TiO_2 and mp-TiO_2/a-SnO_2 ETLs. (b) Imaginary part of IMVS spectra for mp-TiO_2 and mp-TiO_2/a-SnO_2 ETL. The measurements are performed at open circuit voltage and for different bias level of illumination. The complex voltage measured at this conditions, reflects the dynamics of charges recombining in the device